Open Access

Catalysis Research

LIDSEN Publishing Inc.

Original Research

Preparation of a Novel $Bi_2MoO_6/Ag/Ag_2CrO_4$ Catalyst with Promoted Visible Light Photodegradation of RhB Dye

Rui Wang [1, †], Dong Lin [1, †], Minghuan Gao [1], Linna Guo [1, *], Tiesheng Li [1, *], Minghua Liu [2, 3, *]

1. College of Chemistry, Zhengzhou University, 75 North University Road, Zhengzhou, P. R. China; E-Mails: 1130203348@qq.com; 836977016@qq.com; 260065610@qq.com; guolinna@zzu.edu.cn; lts34@zzu.edu.cn
2. Henan Institute of Advanced Technology, Zhengzhou University, Zhengzhou, Henan Province, P.R. China; E-Mail: liumh@iccas.ac.cn
3. Beijing National Laboratory for Molecular Science, Institute of Chemistry, Chinese Academy of Sciences, Zhongguancun North First Street 2, Beijing, P. R. China

† These authors contributed equally to this work.

* **Correspondences:** Linna Guo, Tiesheng Li and Minghua Liu; E-Mails: guolinna@zzu.edu.cn; lts34@zzu.edu.cn; liumh@iccas.ac.cn

Academic Editor: Md Ariful Ahsan

Special Issue: Applications of Environmental

Catalysis Research
2022, volume 2, issue 2
doi:10.21926/cr.2202008

Received: January 29, 2022
Accepted: March 28, 2022
Published: April 07, 2022

Abstract

A series of novel **$Bi_2MoO_6/Ag/Ag_2CrO_4$** heterostructure photocatalysts (denoted as **BA-X**, X = 1, 3, 5, 10) were synthesized using a coprecipitation method. These photocatalysts were characterized by scanning electron microscopy (SEM), X-ray diffraction (XRD), UV-vis spectroscopy, and X-ray photoelectron spectroscopy (XPS) and their photocatalytic properties were investigated. Compared with pure Bi_2MoO_6 or Ag_2CrO_4, **BA-5** exhibited a higher photocatalytic property and broader light absorption. In addition, the surface plasmon resonance (SPR) effect of Ag enhanced the separation of photogenerated carriers. **BA-5** could be recycled at least five times, and XRD and SEM of **BA-5** during the cycles were measured, revealing that the crystal structure and morphology were changed with the increase in the number of cycles. The trapping agent experiments indicated that the holes had a more decisive impact on the degradation of RhB; the degradation mechanism was proposed as Type I.

Keywords
Photocatalysis; heterojunction; **$Bi_2MoO_6/Ag/Ag_2CrO_4$**; photodegradation; pollution

1. Introduction

With the development of several industries, environmental pollution has attracted considerable attention. Untreated industrial wastewater contains numerous organic pollutants that are discharged into the river, thus posing a severe threat to the ecological environment [1-4]. So far, these organic pollutants are degraded by adsorption degradation, photodegradation, and biological method [5-10]. Photodegradation has the unique advantage of high efficiency, and visible light photocatalyst has emerged as the mainstream of research due to its effectiveness in using visible light [11-15].

Bi_2MoO_6, having a low bandgap (2.4-2.8 eV), has gradually attracted the attention of researchers because of its effective utilization of visible light [16, 17]. Zhang et al. obtained a series of Bi_2MoO_6 with different morphologies by changing the pH in a hydrothermal manner [18]. Photocatalytic property of degradation of dyes by Bi_2MoO_6 with other pH values of the solution was investigated，that revealed different degradation efficiencies. Nevertheless, Bi_2MoO_6 is still confronted with low quantum yield and low photocatalytic activity under visible light irradiation [19-24].

Researchers have tried to explore several methods to enhance photocatalytic activity, such as by supporting precious metal nanoparticles and constructing heterojunctions [25-29]. The heterojunction can effectively inhibit the recombination of electrons and holes and enhance photocatalytic activity [30-34]. For example, Li et al. successfully designed and prepared heterojunctions, which exhibited a high photocatalytic ability to degrade RhB under solar light irradiation [35-40].

Silver-based photocatalysts have been extensively investigated [41-47]. Ag_2CrO_4 is an ideal semiconductor with an appropriate bandgap (1.75 eV) and better visible light photocatalytic activity [48]. Ouyang et al. [49] prepared $AgAlO_2$, $AgCrO_2$, and Ag_2CrO_4 using the cation exchange method. The photo-oxidation of MO and gaseous benzene catalyzed by $AgAlO_2$, $AgCrO_2$, and Ag_2CrO_4 was investigated. The activity order of the two reactions is $Ag_2CrO_4 > AgAlO_2 > AgCrO_2$. Moreover, heterojunctions composed of Bi_2MoO_6/silver-based photocatalysts used for photodegrading dyes were reported [50-52]. However, **$Bi_2MoO_6/Ag/Ag_2CrO_4$** having a heterostructure as a photocatalyst has not been studied.

Herein, a series of new **$Bi_2MoO_6/Ag/Ag_2CrO_4$** photocatalysts were prepared, and their photodegradation properties for degrading RhB under visible light irradiation were systematically investigated.

2. Materials and Methods

2.1 Materials

Ethylene glycol (EG) was commercially purchased from Sinopharm Chemical Reagent Co., Ltd. (Shanghai, China). Silver nitrate ($AgNO_3$), bismuth nitrate pentahydrate ($Bi_2(NO_3)_3·5H_2O$), sodium molybdate dihydrate ($Na_2MoO_4·2H_2O$), potassium chromate (K_2CrO_4), polyethylene glycol (PEG), and RhB were commercially purchased from Shanghai Aladdin Biochemical Technology Co., Ltd. (Shanghai, China). All chemicals (analytical grade) were purchased from a commercial market and used as received without any further purification.

2.2 Synthesis of Bi_2MoO_6

In total, 0.97 g of $Bi_2(NO_3)_3·5H_2O$ and 0.24 g of $Na_2MoO_4·2H_2O$ were dissolved in 5 mL of EG, separately and mixed. Next, 20 mL of ethanol was added to the solutions under magnetic stirring until they were dissolved completely. Ammonia was added drop-by-drop to the solution, and the pH was adjusted to 3, 5, 7, and 9. Afterward, the solutions were placed into a 50 mL Teflon-lined stainless autoclave. The autoclave was sealed and maintained at 160 °C for 20 h. After cooling to room temperature, the products were washed with DI and ethanol thrice. Finally, faint yellow Bi_2MoO_6 powders obtained at different pH values of 3, 5, 7, and 9 were dried in a 60 °C vacuum oven for 12 h [18, 32, 53-56].

2.3 Preparation of $Bi_2MoO_6/Ag/Ag_2CrO_4$

In total, 0.10 g (0.5 mmol) of K_2CrO_4 was dissolved in 20 mL of DI until it was dissolved completely. Next, 2 g of PEG 4000 was added to the solution under magnetic stirring until it was dissolved completely. A certain mass proportion of Bi_2MoO_6 1%, 3%, 5%, 10% (1.66 mg, 5.0 mg, 8.3 mg, 16.6 mg, respectively) was added and subjected to ultrasound for 30 min to evenly disperse the mixture. Afterward, 0.17 g (1 mmol) of $AgNO_3$ was added to the dispersion of Bi_2MoO_6 and stirred in the dark for 4 h. Finally, **$Bi_2MoO_6/Ag/Ag_2CrO_4$** composite materials were obtained by washing with deionized water and ethanol thrice and dried in a 60 °C vacuum oven for 12 h [57]. **$Bi_2MoO_6/Ag/Ag_2CrO_4$** with different dosages of Bi_2MoO_6 were labeled as **BA-1**, **BA-3**, **BA-5,** and **BA-10**. Calcination of BA-5 and BA-10 was performed at 550 °C for 2 h in a muffle furnace [58].

2.4 Characterizations

The microstructure and elemental composition of Bi_2MoO_6, Ag_2CrO_4, and the **BA-X** series (ratio: X = 1, 3, 5, 10) were investigated by scanning electron microscopy (SEM ; Hitachi S-4700) and energy-dispersive X-ray spectroscopy (EDX Bruker). Diffuse reflectance spectroscopy (DRS) in the region of 300-800 nm was performed using a PerkinElmer Lambda 950 spectrometer, whereas $BaSO_4$ was selected for background measurements. X-ray diffraction (XRD) was performed on a Bruker D8 VENTURE diffractometer (Bruker, Germany) using Cu-Ka radiation. Photoluminescence (PL) spectra were obtained by an F-4600 fluorescence spectrophotometer with an excitation wavelength of 460 nm. The photoelectron chemical measurements were performed with an electrochemical system (CHI-660D) at room temperature. In these systems, a 1 cm^2 Pt sheet and a saturated calomel electrode (SCE) were employed as the counter and reference electrodes, respectively. Indium-Tin Oxide(ITO) glass electrodes were seared by as-prepared samples (Bi_2MoO_6, Ag_2CrO_4, and **BA-5**) as the working electrode.

2.5 Photocatalytic Test

The photocatalytic activity of the prepared catalyst was assessed by degrading RhB (10 ppm) under the irradiation of a 350 W Xenon lamp. First, 5 mg of RhB was weighed and dispersed in 500 mL of deionized water to obtain the RhB aqueous solution. Next, 30 mg of the photocatalyst was weighed and evenly dispersed in 30 mL of the RhB solution and stirred in darkness for 1 h to achieve the dynamic equilibrium of adsorption and desorption. Afterward, it was stirred under the Xenon lamp irradiation for 1 h, and 3 mL of the solution was absorbed every 10 min. The extracted solution was centrifuged in a high-speed centrifuge, and the supernatant was absorbed as a sample for subsequent testing. Finally, the concentration of RhB in the supernatant was determined by ultravioletvisible spectrophotometry. The experimental process of o-chlorophenol and p-chlorophenol solution photodegradation was similar to that of RhB degradation, such that the pre-configured 10 ppm *o*-chlorophenol, *p*-chlorophenol, MO, MB, and tetracycline solution were degraded under a Xenon lamp. Finally, the concentration of pollutants in the supernatant was determined by high-performance liquid chromatography.

2.6 Recycle Experiment

The photocatalyst was collected from the remaining solution after the reaction was over by centrifuging and washed with water several times. The photocatalyst treated above was added to 30 mL of RhB (10 ppm solution) again. Recycling experiments were repeated until the photocatalyst lost its degradation ability.

3. Results and Discussion

3.1 Characterization of Photocatalysts

3.1.1 Characterization of Bi_2MoO_6 Prepared with Different pH Values

The XRD patterns of Bi_2MoO_6 synthesized at different pH values were measured, as shown in Figure 1. The peaks at 28.2°, 32.5°, 47.1°, 56.2°, 58.4°, 68.1°, 76.0,° and 77.6° belonged to (131), (200), (062), (191), (262), (400), (391), and (402) facets, respectively, of Bi_2MoO_6 (JCPDS No. 76-2388) [59]. No new peaks were detected, indicating that Bi_2MoO_6 had a higher purity. Moreover, the position of diffraction peaks did not change as compared with Bi_2MoO_6 prepared at different pH values, indicating that the change in pH values did not affect the crystal structure of Bi_2MoO_6.

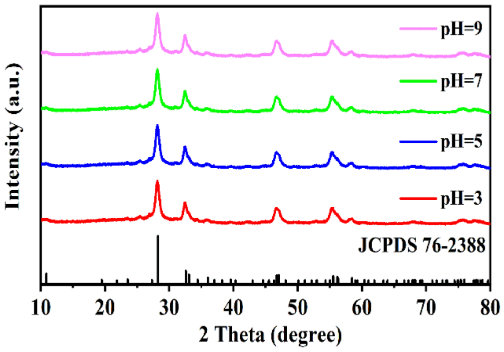

Figure 1 XRD patterns of Bi_2MoO_6 prepared at different pH values (3, 5, 7, and 9).

Morphologies of Bi_2MoO_6 synthesized at various pH (3, 5, 7, and 9) values were measured by SEM, as depicted in Figure 2. Spherical images of Bi_2MoO_6 with an average diameter of about 2 µm were observed (Figure 2a, pH = 3). Several thin sheets on the spherical surface were slowly dispersed, and the spherical morphology was slowly destroyed with an increase in the pH value (Figure 2b, c; pH = 5,7). Finally, the spherical structure disappeared completely, and the flakes with a width of 300 nm and a thickness of 80 nm appeared (Figure 2d; pH = 9). The results obtained above indicated that the morphology of Bi_2MoO_6 could be controlled by changing the pH.

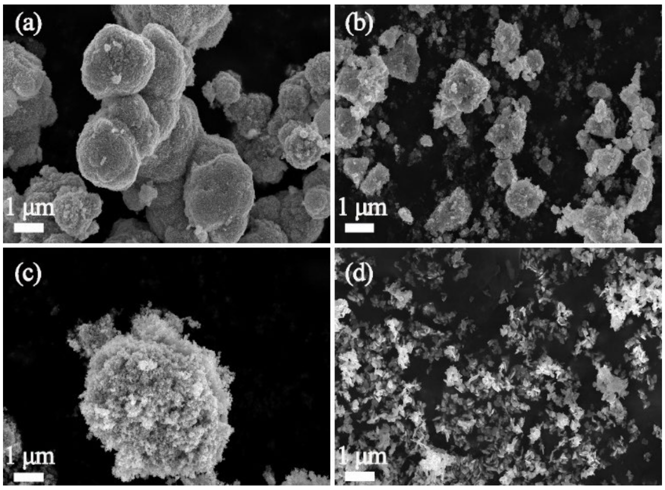

Figure 2 SEM images of Bi_2MoO_6 prepared with different pH values. (a) 3, (b) 5, (c) 7, and (d) 9.

3.2 Characterization of $Bi_2MoO_6/Ag/Ag_2CrO_4$ (BA-X, X = 1, 3, 5 and 10)

The XRD patterns of Bi_2MoO_6, Ag_2CrO_4, and **$Bi_2MoO_6/Ag/Ag_2CrO_4$** were measured, as shown in Figure 3. Peaks at 31.0°, 31.1°, 31.4°, 32.3°, 33.7°, 35.1°, 39.3°, 44.3°, 45.4°, 48.0°, 52.1°, 56.4°, 57.1°, 62.6°, 65.0,° and 67.6° were determined as (220), (031), (211), (002), (131), (221), (122), (240), (222), (051), (400), (160), (213), (402), (062), and (004) facets, respectively, for Ag_2CrO_4 (PDF #26-0952) [57]. The XRD patterns of **$Bi_2MoO_6/Ag/Ag_2CrO_4$** composites were the same as that of Ag_2CrO_4 because of the majority of Ag_2CrO_4 in these composites. However, the intensity of diffraction peaks of the (131) facets at 2θ of 28.2° belonging to Bi_2MoO_6 increased with an increase in the amount of Bi_2MoO_6 doped, suggesting the formation of heterojunction photocatalysts.

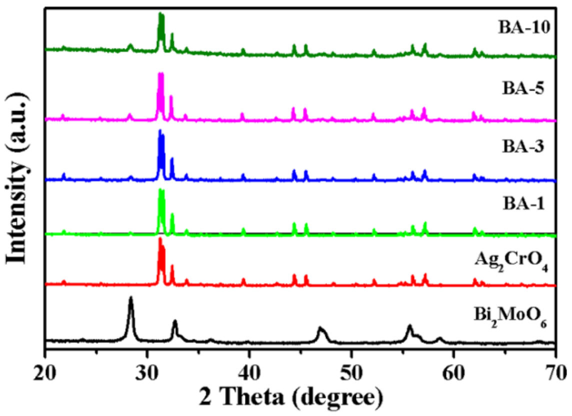

Figure 3 XRD patterns of as-prepared Bi_2MoO_6, Ag_2CrO_4, **BA-1**, **BA-3**, **BA-5**, and **BA-10**.

The SEM images of Ag_2CrO_4 and **BA-X** were measured (Figure 4). The sheets of Bi_2MoO_6 and blocks having a plane length of 200 to 400 nm with a thickness of about 200 nm for Ag_2CrO_4 were observed (Figure 4a, b). The SEM images of **BA-1**, **BA-3**, **BA-5,** and **BA-10** are shown in Figure 4c-f. The images of **BA-X** revealed the bulk morphology of Ag_2CrO_4 and the sheets of Bi_2MoO_6, indicating the formation of heterojunction materials. In addition, an increase in Bi_2MoO_6 resulted in the attachment of more number of Bi_2MoO_6 sheets to the surface of Ag_2CrO_4, which was consistent with our design.

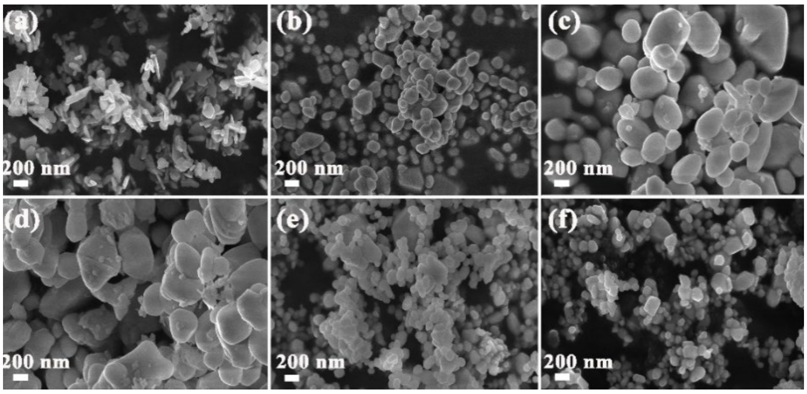

Figure 4 SEM images. (a) Bi_2MoO_6 (pH = 9), (b) Ag_2CrO_4, (c) **BA-1**, (d) **BA-3**, (e) **BA-5,** and (f) **BA-10**.

The TEM and high-magnification HR-TEM characterization images of Bi_2MoO_6 (pH = 9), Ag_2CrO_4, and **BA-5** are shown in Figure 5. It could be seen that Bi_2MoO_6 has a sheet-like structure of about 100 nm (Figure 5a). Its crystal spacing was about d = 0.65 nm in the HR-TEM image, as seen in the upper right corner of the figure. The spherical structure Ag_2CrO_4 has numerous black silver particles fixed on its surface (Figure 5b), and the crystal spacing of Ag_2CrO_4 was about d = 0.350 nm, its crystal plane belonging to (200). The lattice spacing of metal Ag particles was about d = 0.231 nm, and it belonged to the (111) crystal plane. Figure 5c shows the microscopic structure of the composite sample; the microstructure of Bi_2MoO_6 and Ag_2CrO_4, and the HR-TEM image in the upper right corner show that the crystal spacing d = 0.314 nm, d = 0.320 nm, and d = 0.304 nm belonged to the Bi_2MoO_6 (131) crystal plane, d = 0.268 nm and d = 0.249 nm belonged to the Ag_2CrO_4 (002), (200) crystal plane, and d = 0.198 nm belonged to the (111) crystal plane of metal Ag particles. The above results demonstrate the formation of a heterojunction between Bi_2MoO_6 and Ag/Ag_2CrO_4, and the formation of a homojunction between metal Ag and Ag_2CrO_4, indicating that the composite material was successfully prepared.

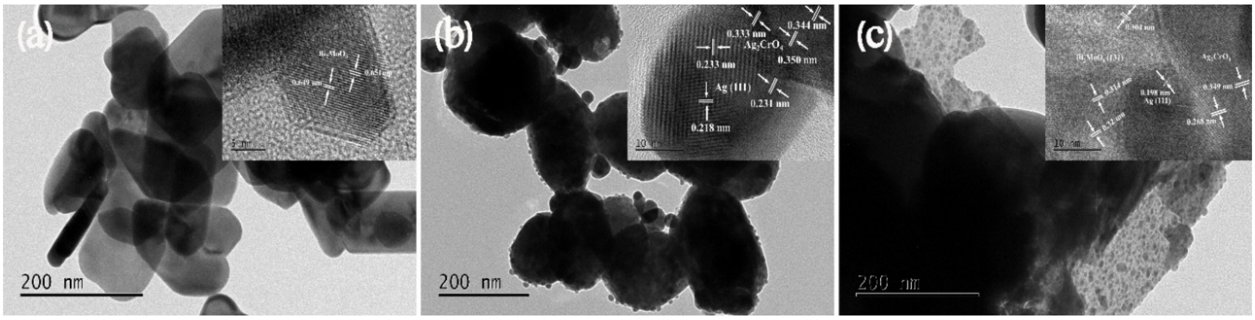

Figure 5 TEM images. (a) Bi_2MoO_6 (pH = 9), (b) Ag_2CrO_4, and (c) **BA-5.**

Nitrogen adsorption--desorption isotherms of Bi_2MoO_6, Ag_2CrO_4, and **BA-5** were measured (Figure 6a), and the relative pore size distributions (RPSD) were obtained (Figure 6b). The pristine Bi_2MoO_6 yielded a type IV isotherm having an H2 hysteresis loop, indicating the mesoporous nature of the material. Ag_2CrO_4 exhibited a type III isotherm having an approximate H3 hysteresis loop, indicating a narrow gap. **BA-5** showed a type III shape and H3 hysteresis loop [35, 60]. The results showed that the addition of even a small amount of Bi_2MoO_6 maintained the primary structure of **BA-5**. The specific surface areas for Bi_2MoO_6, Ag_2CrO_4, and **BA-5** were 22.74 $m^2\ g^{-1}$, 3.60 $m^2\ g,^{-1}$, and 4.88 $m^2\ g^{-1}$, respectively (Figure 6b). **BA-5** had a larger specific surface area compared with Ag_2CrO_4, indicating that a small amount of Bi_2MoO_6 doped led to more active centers in its heterostructure, which could further enhance its photocatalytic activity. The RPSD of Bi_2MoO_6, Ag_2CrO_4, and **BA-5** were 21.52 nm, 9.65 nm, and 11.66 nm for Bi_2MoO_6, Ag_2CrO_4, and **BA-5**, indicating the mesoporous nature of materials (Figure 6b).

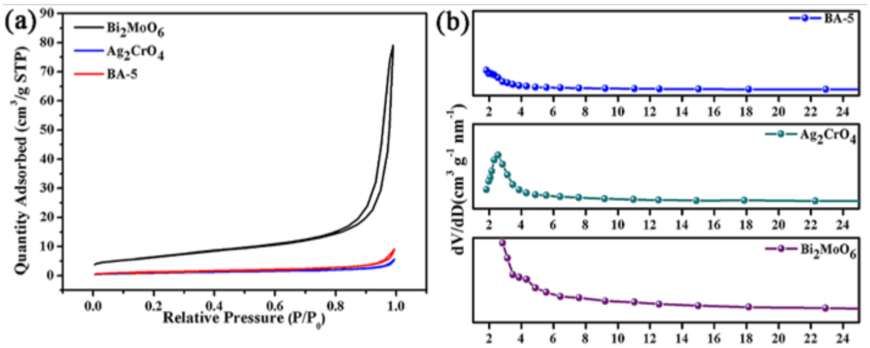

Figure 6 (a) N_2 adsorption--desorption isotherms and (b) the relative pore size distribution of Bi_2MoO_6, Ag_2CrO_4, and **BA-5**.

X-ray photoelectron spectroscopy (XPS) could be used to investigate the element composition and valence [35]. The XPS survey spectra of **BA-5**, Bi_2MoO_6, and Ag_2CrO_4 were measured, as shown in Figure 7. High-resolution XPS spectra of Ag 3d, Cr 2p, Bi 4f, and Mo 3d are shown in Figure 8. Ag, Cr, Bi, Mo, and O elements in **BA-5** could be observed in the survey (Figure 7). The BE peaks at 367.62 eV and 373.60 eV were denoted to Ag 3d$_{5/2}$ and Ag 3d$_{3/2}$, indicating the existence of metallic Ag and Ag^{+} in high-resolution XPS (Figure 8a). The BE peaks at 578.76 eV and 588.19 eV were denoted to Cr 2P$_{3/2}$ and Cr 2p$_{1/2}$ in Figure 8b, indicating that the valence state was +6. The BE peaks at 158.98 eV and 164.29 eV were classified as Bi 4F$_{7/2}$ and Bi 4F$_{5/2}$, and their valence states were Bi^{3+} (Figure 8c). Figure 8d showed that the characteristic BE peaks at 232.26 eV and 235.51 eV were 3d$_{3/2}$ and 3d$_{5/2}$ of Mo having +6 valence.

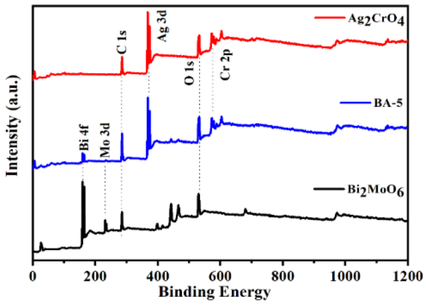

Figure 7 XPS survey spectra of the **BA-5**, Bi_2MoO_6, and Ag_2CrO_4.

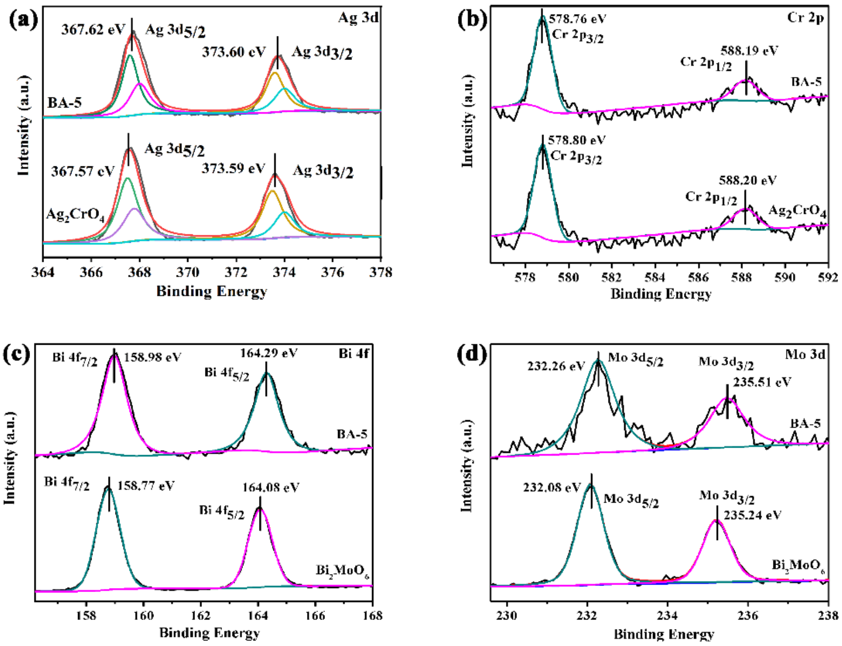

Figure 8 High-resolution XPS spectra of (a) Ag 3d, (b) Cr 2p, (c) Bi 4f, and (d) Mo 3d.

The optical absorption is related to the electronic structure of the semiconductor [28, 32]. UV spectra of **BA-X** (X = 1, 3, 5, 10), Bi_2MoO_6, and Ag_2CrO_4. were assessed to determine the light absorption range. As shown in Figure 9a, a weak absorption in the visible region for Bi_2MoO_6 was observed. Ag_2CrO_4 had a stronger absorption ranging from 500 to 680 nm. However, the light absorption range of **BA-5** was similar to that of Ag_2CrO_4, which was caused by doping Bi_2MoO_6. The bandgap widths for Bi_2MoO_6 and Ag_2CrO_4 were calculated from Figure 9b, in which the Eg values were 2.78 eV and 1.80 eV for Bi_2MoO_6 and Ag_2CrO_4, respectively.

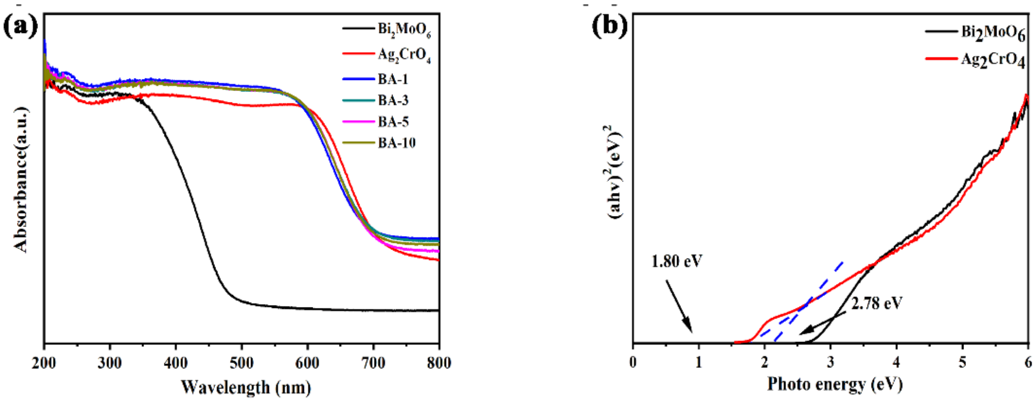

Figure 9 (a) UV diffuse reflectance spectra of pristine Bi_2MoO_6, Ag_2CrO_4, **BA-1, BA-3**, **BA-5**, and **BA-10**. (b) *E*g of pristine Bi_2MoO_6 and Ag_2CrO_4.

To study the electron--hole conversion process of Bi_2MoO_6 and Ag_2CrO_4, the CB of the material was calculated using the equation, $E_{CB} = X - E^{\theta} - 0.5Eg$ (*E*g: the forbidden bandwidth, E^{θ}: the energy of free electrons on the hydrogen scale [4.5 eV], and X: the electronegativity). The X values were 5.55 and 5.86 for Bi_2MoO_6 and Ag_2CrO_4, as reported previously [61-63]. The edge of the VB (E_{VB}) could be obtained from the $E_{VB} = E_{CB} + Eg$ equation. The calculated E_{CB} values of Bi_2MoO_6 and Ag_2CrO_4 were −0.34 eV and 0.46 V, and E_{VB} values were 2.44 eV and 2.26 eV.

3.3 Investigation of Photocatalytic Properties

To obtain **Bi_2MoO_6/Ag/Ag_2CrO_4** with excellent photocatalytic performance, **Bi_2MoO_6** prepared at different pH values was selected to degrade RhB (10 PPM solution) under Xenon lamp irradiation. First, considering the effect of adsorption, the solution of RhB was mixed with Bi_2MoO_6 and stirred for 1 h in the dark to reach absorption-desorption equivalence. In contrast, when the prepared Bi_2MoO_6 pH was 9, the degradation capacity of RhB was better (Figure 10, green line), and the degradation rate reached 22% after irradiation for 1 h. According to the SEM image in Figure 2, the pH value could affect photocatalytic performance by influencing the morphology of Bi_2MoO_6 [18]. When pH = 9, the particle size of Bi_2MoO_6 was small and had more sufficient contact with pollutants. Therefore, Bi_2MoO_6 prepared (at pH = 9) was selected in the following experiment.

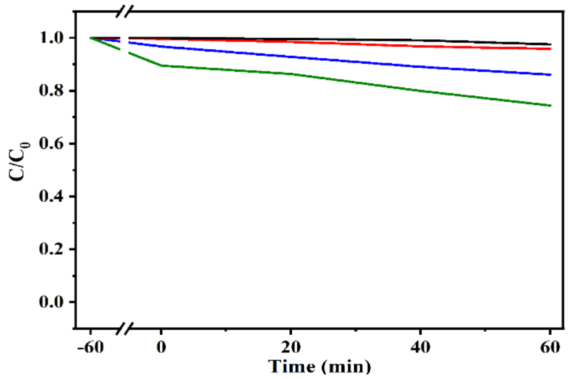

Figure 10 Photocatalytic activity of Bi_2MoO_6 prepared at pH = 3 (blue), 5 (red), 7 (black) and 9 (green) used to degrade RhB (10 ppm solution) under 350 W Xenon lamp irradiation.

Similarly, the photocatalytic properties of **BA-5** (black, blue) and **BA-10** (red, green) with and without calcination were assessed by desorption of RhB (10 ppm solution). Considering the adsorption of pollutants by the catalyst, RhB and **BA-5** or **BA-10** solutions were stirred for 1 h in the dark to reach the adsorption--desorption equilibrium. As shown in Figure 11, the degradation rates of **BA-5** and **BA-10** before and after calcination were almost the same, which could be because calcination did not change the crystal structure of as-prepared **BA-5** and **BA-10** (Figure 12).

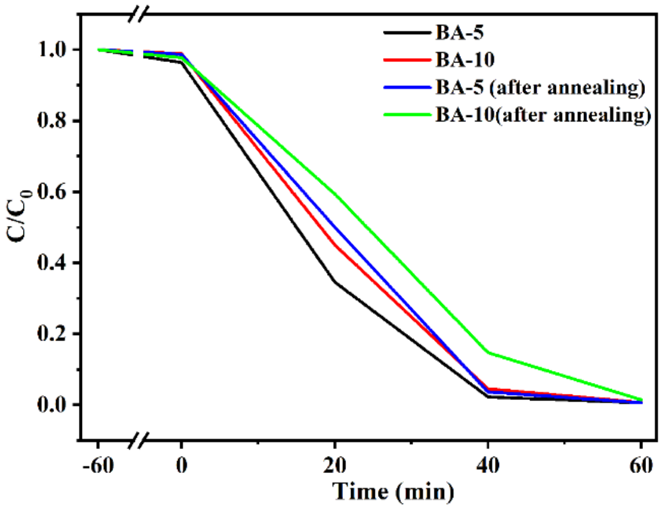

Figure 11 Photocatalytic activity of **BA-5** and **BA-10** prepared before and after calcination at 550 °C for 2 h to degrade RhB (10 ppm solution) under Xenon lamp irradiation.

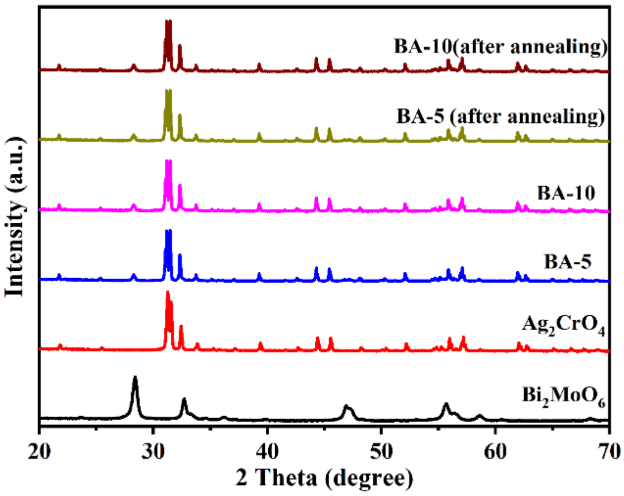

Figure 12 XRD spectra of Bi_2MoO_6/Ag/Ag_2CrO_4 samples prepared before and after calcination at 550 °C for 2 h.

Photocatalytic properties of **BA-1**, **BA-3**, **BA-5**, and **BA-10** were investigated by degrading RhB (Figure 13a). The prepared **BA-X** (X: 1, 3, 5, 10) had more vital photocatalytic degradation ability than Bi_2MoO_6 (pH = 9) and Ag_2CrO_4. **BA-5** and **BA-10** had a high photocatalytic property, and their degradation rate of RhB was up to 99.9% in 60 min, whereas the degradation rates of pure Bi_2MoO_6 (pH = 9) and Ag_2CrO_4 were only 22.0%, and 53.8%, respectively. Figure 13b shows the linear relationship between −ln(C/C0) and t, the degradation curve of RhB was consistent with the pseudo-first-order kinetic equation [64, 65]. The degradation rate constant k_{ap} of BA-5 was 0.07857 min^{-1}, which was 24.63 times of pure Bi_2MoO_6 and 6.44 times of pure Ag_2CrO_4. It indicated that the photocatalytic performance of **Bi_2MoO_6/Ag/Ag_2CrO_4** was considerably higher than that of the pure Bi_2MoO_6 or Ag_2CrO_4 due to the formation of a heterojunction structure.

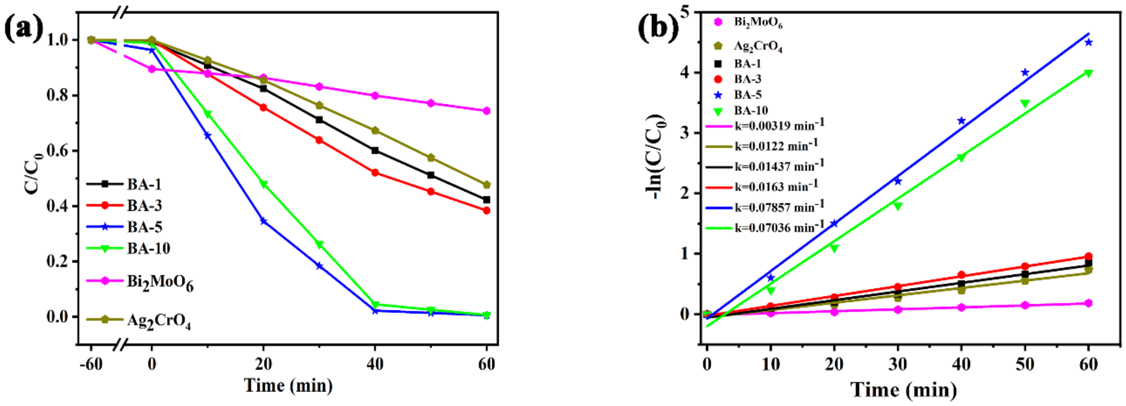

Figure 13 (a) Photocatalytic activity of Bi_2MoO_6 prepared at pH = 9, Ag_2CrO_4, and **BA-X** (X = 1, 3, 5, 10) to degrade RhB (10 ppm solution) under Xenon lamp irradiation. (b) Pseudo first-order kinetic constants of RhB photodegradation.

The photocatalytic performance of BA-5 for decomposing phenol was also investigated under Xe lamp irradiation. The peak intensities of *o*-chlorophenol and *p*-chlorophenol decreased rapidly when irradiated for 1 h, indicating that BA-5 also had a better degrading efficiency for phenol (Figure 14). In addition to the photodegradation of RHB, *o*-chlorophenol, and *p*-chlorophenol, we tried to degrade MB and MO, and the degradation efficiencies were 82.34% and 61.02% in 60 min, respectively. Unfortunately, BA-5 showed a low degradation activity for tetracycline under the same condition.

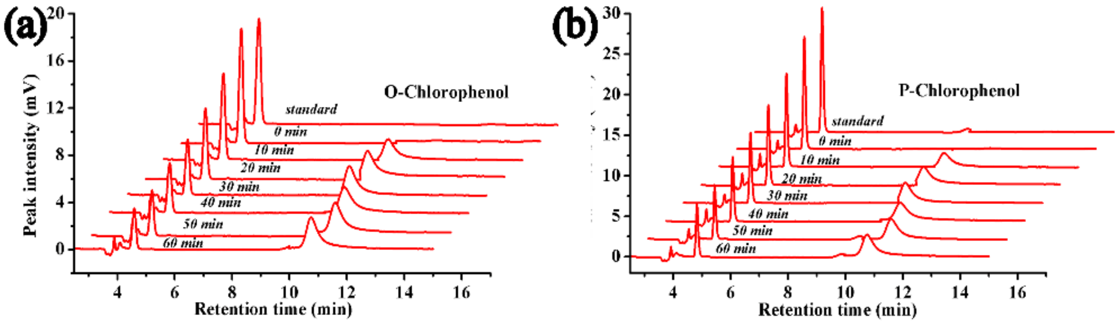

Figure 14 Photocatalytic activities of **BA-5** were characterized under Xenon lamp irradiation at different times by high-performance liquid chromatography (HPLC): (a) *o*-chlorophenol (10 ppm solution) and (b) *p*-chlorophenol (10 ppm solution).

3.4 Photocatalysis Stability

Photostability is one of the important indexes for a catalyst. The recycling capacity and photostability of **BA-5** were systematically studied. The degradation rate of **BA-5** for RhB was up to 99.9% in the first recycle, 87.6% in the second cycle, 74.5% in the third cycle, and 60.2% in the fourth cycle. The degradation rate of **BA-5** for RhB was still up to 51.3% in the fifth recycling (Figure 15), indicating that **BA-5** exhibited a better recycling performance in the photocatalytic process.

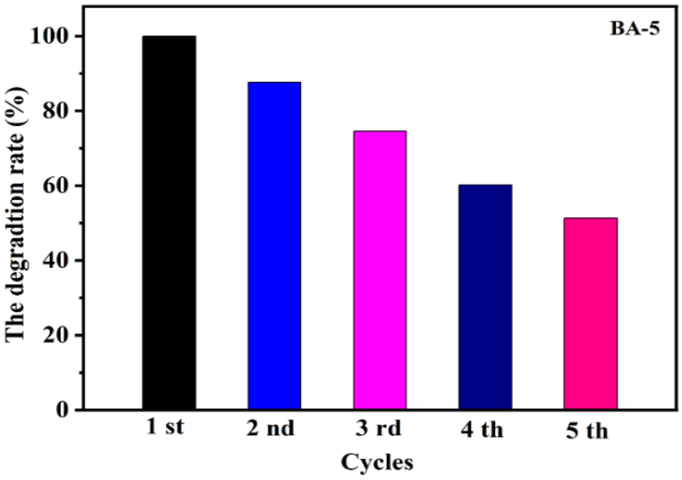

Figure 15 Recycling stability of **BA-5** for degrading RhB irradiated by Xenon lamp.

The photocatalytic activities of **Bi_2MoO_6/Ag/Ag_2CrO_4** compared with other similar photocatalysts reported are listed in Table 1.

Table 1 Comparison with similar photocatalysts for degrading RhB.

NO.	Cat.	Light source	Time (min)	Catalytic substrate	Degradation rate (%)	Cycles (Time)	Ref.
1	Bi_2MoO_6/Ag_2CrO_4	Visible-light	60	RhB	99.9	5	This work
2	Bi_2MoO_6	Visible-light	100	RhB	99.9	-	[19]
3	Bi_2MoO_6	Visible-light	120	RhB	98.2	5	[17]
4	$g\text{-}C_3N_4/Bi_2MoO_6$	Visible-light	70	RhB	98.0	8	[35]
5	$AgBr/Ag_2CrO_4$	Visible-light	40	RhB	93	-	[51]
6	$BiIO_4/Bi_2MoO_6$	Visible-light	300	RhB	80	-	[61]
7	$Ag_2CrO_4/Bi_2Sn_2O_7$	Visible-light	120	RhB	97.5	5	[52]
8	$PANI_x/Bi_2MoO_6$	Visible-light	120	RhB	99.9	-	[24]
9	AgI/Bi_2MoO_6	Visible-light	40	RhB	92.89	3	[50]
10	$\delta\text{-}Bi_2O_3/Bi_2MO_6$	Visible-light	140	RhB	97.6	-	[36]
11	$Bi_2O_2CO_3/Bi_2MoO_6$	Visible-light	30	RhB	99.9	-	[31]
12	$g\text{-}C_3N_4/Ag_2CrO_4$	Visible-light	90	RhB	99.2	4	[60]

To study the deactivation reason for the degradation of performance, XRD characterization of **BA-5** was measured before and after recycling. The position and intensity of diffraction peaks for 0 min, 10 min, 20 min, 30 min, and 60 min did not change significantly, indicating that the crystal structure of **BA-5** did not change during the degradation process (Figure 16).

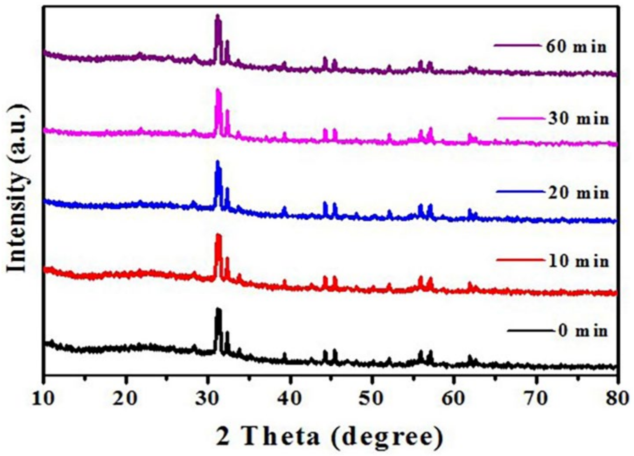

Figure 16 XRD patterns of **BA-5** during the first catalytic process.

XRD tests were performed for five catalytic cycles of **BA-5**. The position and intensity of diffraction peaks of the first and second times did not change significantly. The intensity of diffraction peaks of 31.0°, 31.1°, and 31.4° gradually weakened after the third cycle, indicating that the crystal structure of **BA-5** changed with the increase in the number of cycles (Figure 17).

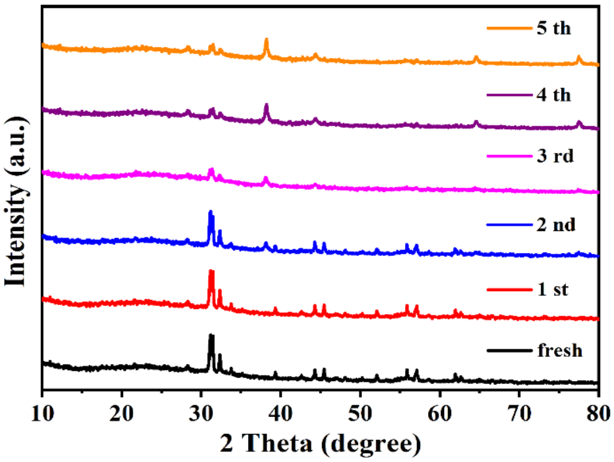

Figure 17 XRD patterns of **BA-5** in five catalytic processes.

To observe the morphological changes of samples during the degradation process, SEM images of **BA-5** during the process were characterized (Figure 18). Morphologies of **BA-5** did not change significantly during degradation, indicating that **BA-5** had excellent stability. Compared with Figure 18a and Figure 18i, the morphology of **BA-5** changed considerably in the fifth cycle. Therefore, the more significant change in morphology was one of the reasons for the decreased activity.

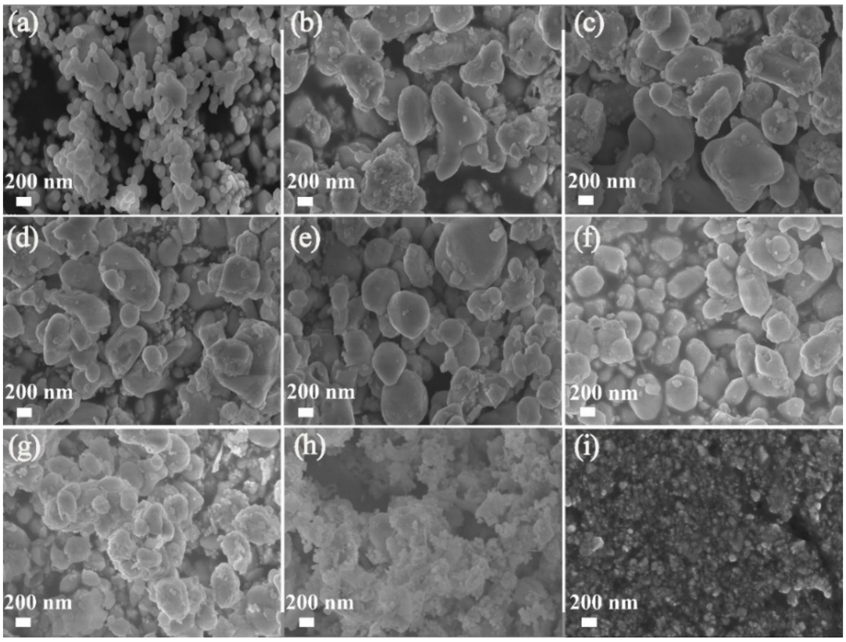

Figure 18 SEM image of **BA-5** during catalytic process under Xenon lamp irradiation. (a) 0 min, (b) 10 min, (c) 20 min, (d) 30 min, (e) 60 min, (f) SEM image of **BA-5** after 2 cycles, (g) after 3 cycles, (h) after 4 cycles, and (i) after 5 cycles.

3.5 Investigation of the Photocatalytic Mechanism

3.5.1 Catalytic Active Species in $Bi_2MoO_6/Ag/Ag_2CrO_4$

Various scavengers, such as isopropyl alcohol (IPA), benzoquinone (BQ), and triethanolamine (TEOA), were applied to the photodegradation of RhB to elucidate what reactive species were the key influencing factors. As shown in Figure 19, the degradation was inhibited completely by adding TEOA, meaning that hole (h^+) was the main influencing factor. In the case of BQ ($\bullet O_2^-$) and IPA ($\bullet OH$), less effect was observed in the photocatalytic progress, and the degradation rates were 66.8% and 77.0%. The results indicated that the hole (h^+) played the most crucial role in the whole degradation process [66].

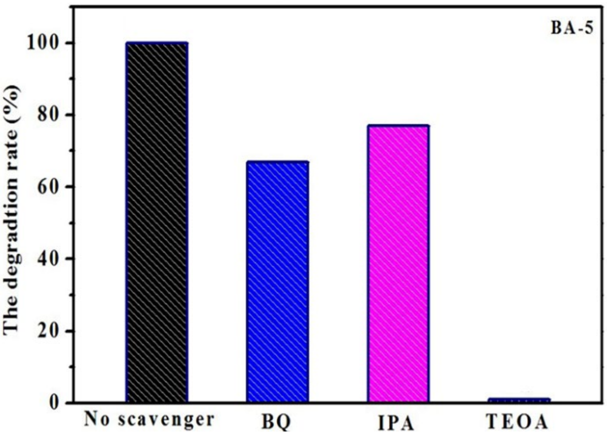

Figure 19 Capture experiments for **BA-5** to photodegrade RhB under Xenon lamp irradiation.

3.5.2 Photoluminescence Spectra

The recombination rate of electron--hole pairs during the photodegradation process was explored with the PL spectra. The fluorescence spectra of Bi_2MoO_6, Ag_2CrO_4, and **BA-5** were recorded (Figure 20), and the wide emission peak of pure $Bi_2MoO_6$was observed at around 465 nm, which was attributed to its rapid electron--hole recombination (Figure 20, black line). Pure Ag_2CrO_4 had a low recombination efficiency (Figure 20, red line) [66]. The emission peak of **BA-5** was similar to that of pure Ag_2CrO_4 after the combination; however, the luminous position of **BA-5** was weaker than that of Bi_2MoO_6 and Ag_2CrO_4, indicating that the combination of BA-5 had a low photogenerated carrier recombination efficiency (Figure 20, blue line) [66]. The result showed that **BA-5** had lower recombination of the photoexcited electron-holes due to the formation of a heterojunction.

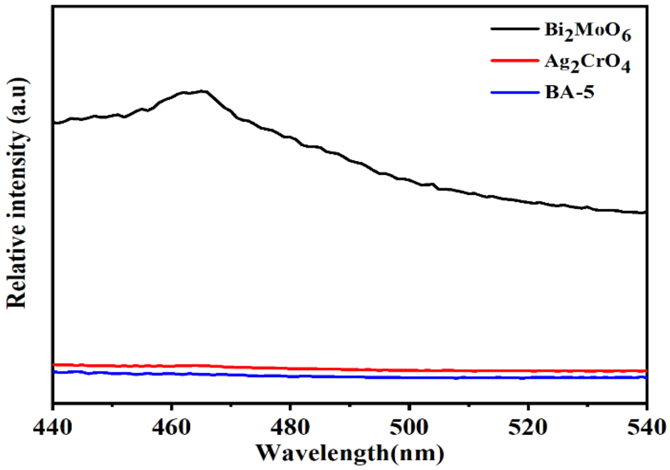

Figure 20 Photoluminescence emission spectra of Bi_2MoO_6 (black line), Ag_2CrO_4 (red line), and **BA-5** (blue line).

The separation of electron--hole in the photocatalyst was studied by the photocurrent method. Generally, a higher photocatalytic degradation ability was associated with higher photocurrent property of the photocatalyst. The transient photocurrent response diagrams of Ag_2CrO_4, Bi_2MoO_6, and **BA-5** under optical switching conditions were measured (Figure 21). **BA-5** had a higher separation and transfer efficiency of photogenerated electron--hole pairs under visible light irradiation; the photocurrent response of the **BA-5** composites increased significantly in comparison with that of pure Ag_2CrO_4 and Bi_2MoO_6, and hence the higher photocatalytic activity (Figure 21a, blue line). Electrochemical impedance experiments wereperformed on Ag_2CrO_4, Bi_2MoO_6, and **BA-5** (Figure 21b), which showed the semicircular curves in the intermediate frequency region, in which **BA-5** had the smallest arc radius. **BA-5** had a high charge carrying rate and slow charge separation, showing that the heterojunction structure could effectively enhance the separation of charge carriers.

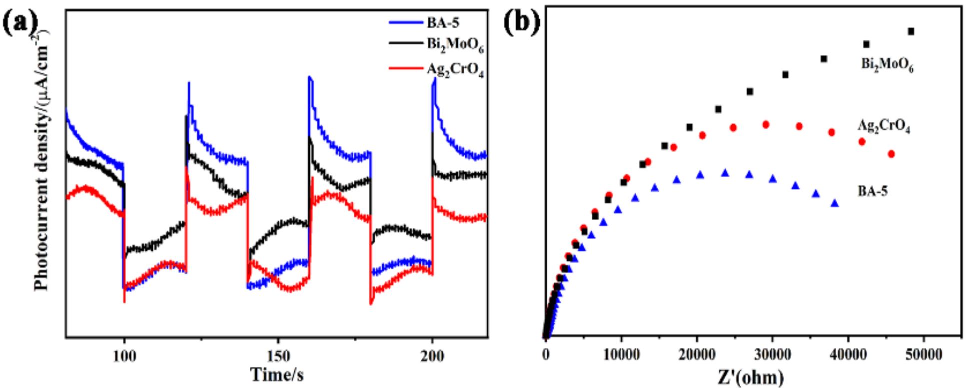

Figure 21 (a) Typical transient photocurrent responses diagrams of Ag_2CrO_4 (red), Bi_2MoO_6 (black), and **BA-5** (blue) deposited on the ITO electrodes under intermittent UV-visible irradiation. (b) Typical electrochemical impedance diagrams of Ag_2CrO_4, Bi_2MoO_6, and **BA-5** deposited on ITO electrodes.

3.5.3 Proposal Photodegradation Mechanism

The process of charge carrier transfer was proposed according to the valence states and CB positions of Ag_2CrO_4 and Bi_2MoO_6 (Figure 22). **$Bi_2MoO_6/Ag/Ag_2CrO_4$** could be judged as a Type I in the coupling process. Under light irradiation, the photogenerated electrons in the conduction band (CB) of Bi_2MoO_6 were transferred to the conduction band (CB) of Ag_2CrO_4 due to the higher stabilization with the lower potential energy of Bi_2MoO_6. From the capture experiment (Figure 19), it was inferred that a small amount of •OH and $•O_2^-$ were involved, whereas the VB edge potential (2.26 eV) and the CB edge potential (0.46 eV) of Ag_2CrO_4 were lower than $•OH/H_2O$ (2.4 eV) and $O_2/•O_2^-$ (-0.046 eV), respectively. Thus, the holes in the valence band (VB) of Ag_2CrO_4 could not oxidize H_2O to •OH, and the photogenerated electrons in CB could not reduce O_2 to $•O_2^-$. Although the potential at the edge of VB (2.44 eV) and CB (−0.34 eV) of Bi_2MoO_6 was higher than at $•OH/H_2O$ (2.4 eV) and $O_2/•O_2^-$ (−0.046 eV), the holes in the VB of Bi_2MoO_6 oxidized H_2O to •OH, and the photogenerated electrons in CB reduced O_2 to $•O_2^-$. Most importantly, the holes in the VB of Ag_2CrO_4 participated in the degradation of organic pollutants. Simultaneously, the surface plasmon resonance (SPR) effect of the metallic Ag facilitated electron transfer in the homojunction structure.

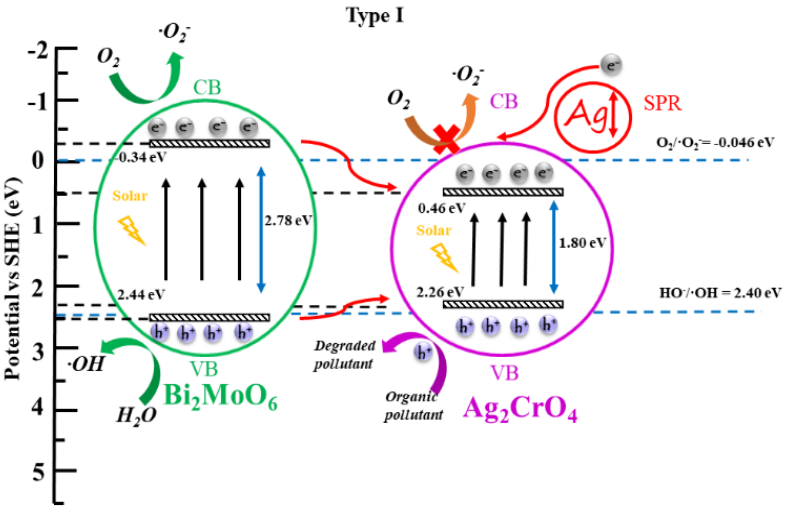

Figure 22 Plausible photocatalytic mechanism.

4. Conclusions

Several morphologies of Bi_2MoO_6 were prepared at different pH values using a hydrothermal method. Bi_2MoO_6 was prepared at pH 9 and had the best degradation effect on RhB, showing that the morphology could affect their photocatalytic performance. A series of **$Bi_2MoO_6/Ag/Ag_2CrO_4$** photocatalysts were synthesized and characterized. The photocatalytic performance of **$Bi_2MoO_6/Ag/Ag_2CrO_4$** used to degrade RhB under irradiation was investigated. Trapping agent experiments showed that holes played an essential role in the degradation of RhB, and the degradation mechanism was proposed as Type I. Furthermore, **BA-5** had better stability and could be reused at least five times. With the increase in the number of cycles, the intensity of the diffraction peak corresponding to the XRD of the catalyst weakened, indicating a change in the crystal structure of the catalyst. The morphology of the catalyst had changed significantly through the SEM. Therefore, **BA-5** had the best catalytic performance due to its excellent light absorption and high carrier separation efficiency. The enhanced performance could be ascribed to the **$Bi_2MoO_6/Ag/Ag_2CrO_4$** structure, improved charge transfer efficiency, and suppressed photoelectron−hole recombination.

Author Contributions

Rui Wang was responsible for data analysis and manuscript writing; Dong Lin was in charge of instrument operation; Minghuan Gao was responsible for the experimental design; Linna Guo and Tiesheng Li were responsible for providing the overall experimental idea.

Funding

This work was supported by the National Natural Science Foundation of China (21861132002) and the Henan Natural Science Foundation of China (192102210046).

Competing Interests

The authors have declared that no competing interests exist.

References

1. Shi JX, Huang WP, Han HJ, Xu CY. Pollution control of wastewater from the coal chemical industry in China: Environmental management policy and technical standards. Renew Sustain Energy Rev. 2021; 143: 110883.
2. Agustina TE, Ang HM, Vareek VK. A review of synergistic effect of photocatalysis and ozonation on wastewater treatment. J Photochem Photobiol C. 2005; 6: 264-273.
3. Ali H, Mansor ES. Co-sensitization of mesoporous ZnS with CdS and polyaniline for efficient photocatalytic degradation of anionic and cationic dyes. Colloids Interface Sci Commun. 2020; 39: 100330.
4. Zafiu C, Part F, Ehmoser EK, Kahkonen MA. Investigations on inhibitory effects of nickel and cobalt salts on the decolorization of textile dyes by the white rot fungus Phanerochaete velutina. Ecotoxicol Environ Saf. 2021; 215: 112093.
5. Alfano OM, Bahnemann D, Cassano AE, Dillert R, Goslich R. Photocatalysis in water environments using artificial and solar light. Catal Today. 2000; 58: 199-230.
6. Fujishima A, Rao TN, Tryk DA. Titanium dioxide photocatalysis. J Photochem Photobiol C. 2000; 1: 1-21.
7. Qin SJ, Gan JY, Liu WP, Becker JO. Degradation and adsorption of Fosthiazate in soil. J Agric Food Chem. 2004; 52: 6239-6242.
8. Pan M, Chu LM. Adsorption and degradation of five selected antibiotics in agricultural soil. Sci Total Environ. 2016; 545: 48-56.
9. Badawy MI, Wahaab RA, El-Kalliny AS. Fenton-biological treatment processes for the removal of some pharmaceuticals from industrial wastewater. J Hazard Mater. 2009; 167: 567-574.
10. Rosal R, Rodríguez A, Perdigón-Melón JA, Petre A, García-Calvo E, Gómez MJ, et al. Occurrence of emerging pollutants in urban wastewater and their removal through biological treatment followed by ozonation. Water Res. 2010; 44: 578-588.
11. Mills A, Hunte SL. An overview of semiconductor photocatalysis. J Photochem Photobiol A. 1997; 108: 1-35.
12. Saeed M, Muneer M, Haq AU, Akram N. Photocatalysis: An effective tool for photodegradation of dyes-a review. Environ Sci Pollut Res. 2022; 29: 293-311.
13. Khan I, Sun N, Wang Y, Li Z, Qu Y, Jing L. Synthesis of SnO_2/yolk-shell $LaFeO_3$ nanocomposites as efficient visible-light photocatalysts for 2,4-dichlorophenol degradation. Mater Res Bull. 2020; 127: 110857.
14. Fan Z, Meng F, Zhang M, Wu Z, Sun Z, Li A. Solvothermal synthesis of hierarchical TiO_2 nanostructures with tunable morphology and enhanced photocatalytic activity. Appl Surf Sci. 2016; 360: 298-305.
15. Al-Fahdi T, Al Marzouqi F, Kuvarega AT, Mamba BB, Al Kindy SM, Kim Y, et al. Visible light active CdS@TiO_2 core-shell nanostructures for the photodegradation of chlorophenols. J Photochem Photobiol A. 2019; 374: 75-83.
16. Yu H, Zhu Z, Zhou J, Wang J, Li J, Zhang Y. Self-assembly and enhanced visible-light-driven photocatalytic activities of Bi_2MoO_6 by tungsten substitution. Appl Surf Sci. 2013; 265: 424-

430.

17. Dumrongrojthanath P, Thongtem T, Phuruangrat A, Thongtem S. Glycolthermal synthesis of Bi_2MoO_6 nanoplates and their photocatalytic performance. Mater Lett. 2015; 154: 180-183.
18. Zhang LW, Xu TG, Zhao X, Zhu YF. Controllable synthesis of Bi_2MoO_6 and effect of morphology and variation in local structure on photocatalytic activities. Appl Catal B. 2010; 98: 138-146.
19. Xie LJ, Ma JF, Xu GJ. Preparation of a novel Bi_2MoO_6 flake-like nanophotocatalyst by molten salt method and evaluation for photocatalytic decomposition of rhodamine B. Mater Chem Phys. 2008; 110: 197-200.
20. Tian GH, Chen YJ, Zhou J, Tian CG, Li R, Wang CJ, et al. In situ growth of Bi_2MoO_6 on reduced graphene oxide nanosheets for improved visible-light photocatalytic activity. CrystEngComm. 2014; 16: 842-849.
21. Lin X, Liu D, Guo XY, Sun N, Zhao S, Chang LM, et al. Fabrication and efficient visible light-induced photocatalytic activity of $Bi_2MoO_6/BiPO_4$ composite. J Phys Chem Solids. 2015; 76: 170-177.
22. Lin XY, Guo X, Liu D, Wang QW, Zhai HJ, Chang LM. SiO_2/Bi_2MoO_6 nanocomposites with high photocatalytic activity under visible light irradiation. Mater Res Bull. 2015; 63: 72-79.
23. Wang ZL, Huo Y, Zhang JF, Lu C, Dai K, Liang CH, et al. Facile preparation of two-dimensional $Bi_2MoO_6@Ag_2MoO_4$ core-shell composite with enhanced visible light photocatalytic activity. J Alloys Compd. 2017; 729: 100-108.
24. Feng TT, Yin H, Jiang H, Chai X, Li XL, Li DY, et al. Design and fabrication of polyaniline/Bi_2MoO_6 nanocomposites for enhanced visible-light-driven photocatalysis. New J Chem. 2019; 43: 9606-9613.
25. Nah YC, Paramasivam I, Schmuki P. Doped TiO_2 and TiO_2 nanotubes: Synthesis and applications. ChemPhysChem. 2014; 11: 2698-2713.
26. Shestopal NA, Linnik OP, Smirnova NP. Influence of metal and non-metal ions doping on the structural and photocatalytic properties of titania films. Chem Phys Technol Surf. 2015; 6: 203-210.
27. Reszczyńska J, Grzyb T, Sobczak JW, Lisowski W, Gazda M, Ohtani B, et al. Visible light activity of rare earth metal doped (Er^{3+}, Yb^{3+} or Er^{3+}/Yb^{3+}) titania photocatalysts. Appl Catal B. 2015; 163: 40-49.
28. Peng Y, Wang KK, Liu T, Xu J, Xu BG. Synthesis of one-dimensional Bi_2O_3-$Bi_2O_{2.33}$ heterojunctions with high interface quality for enhanced visible light photocatalysis in degradation of high-concentration phenol and MO dyes. Appl Catal B. 2017; 203: 946-954.
29. Ma ZY, Li PH, Ye LQ, Wang L, Xie HQ, Zhou Y. Selectivity reversal of photocatalytic CO_2 reduction by Pt loading. Catal Sci Technol. 2018; 8: 5129-5132.
30. Medina JC, Portillo-Vélez NS, Bizarro M, Hernández-Gordillo A, Rodil SE. Synergistic effect of supported ZnO/Bi_2O_3 heterojunctions for photocatalysis under visible light. Dyes Pigm. 2018; 153: 106-116.
31. Xu JJ, Yu W, Chen MD, Fei T. A novel BiOCl/BiOCOOH heterojunction photocatalyst with significantly enhanced photocatalytic activity. Mater Lett. 2018; 222: 176-179.
32. Shi WL, Li MY, Huang XL, Ren HJ, Guo F, Tang YB, et al. Construction of $CuBi_2O_4/Bi_2MoO_6$ p-n heterojunction with nanosheets-on-microrods structure for improved photocatalytic activity towards broad-spectrum antibiotics degradation. Chem Eng J. 2020; 394: 125009.
33. Yu B, Wu Y, Meng F, Wang Q, Jia X, Wasim Khan M, et al. Formation of hierarchical

Bi_2MoO_6/In_2S_3 S-scheme heterojunction with rich oxygen vacancies for boosting photocatalytic CO_2 reduction. Chem Eng J. 2022; 429: 132456.

34. Fan Z, Meng F, Gong J, Li H, Hu Y, Liu D. Enhanced photocatalytic activity of hierarchical flower-like CeO_2/TiO_2 heterostructures. Mater Lett. 2016; 175: 36-39.
35. Li HP, Liu JY, Hou WG, Du N, Zhang RJ, Tao XT. Synthesis and characterization of g-C_3N_4/Bi_2MoO_6 heterojunctions with enhanced visible light photocatalytic activity. Appl Catal B. 2014; 160: 89-97.
36. Yin Y, Li F, Zhan QF, Jiang DM, Chen RZ. Synthesis of δ-Bi_2O_3/Bi_2MoO_6 composites with enhanced photocatalytic activity by hydrothermal method. Mater Res Bull. 2018; 103: 47-54.
37. Xu YS, Zhang WD. Anion exchange strategy for construction of sesame-biscuit-like $Bi_2O_2CO_3/Bi_2MoO_6$ nanocomposites with enhanced photocatalytic activity. Appl Catal B. 2013; 140: 306-316.
38. Saeed M, Alwadai N, Ben Farhat L, Baig A, Nabgan W, Iqbal M. Co_3O_4-Bi_2O_3 heterojunction: An effective photocatalyst for photodegradation of rhodamine B dye. Arab J Chem. 2022; 15: 103732.
39. Saeed M, Siddique M, Ibrahim M, Akram N, Usman M, Aleem MA, et al. Calotropis gigantea leaves assisted biosynthesis of ZnO and Ag@ZnO catalysts for degradation of rhodamine B dye in aqueous medium. Environ Prog Sustain Energy. 2020; 39: e13408.
40. Saeed M, Muneer M, Khosa MK, Akram N, Khalid S, Adeel M, et al. Azadirachta indica leaves extract assisted green synthesis of Ag-TiO_2 for degradation of Methylene blue and Rhodamine B dyes in aqueous medium. Green Process Synth. 2019; 8: 659-666.
41. Gao R, Song JM, Hu YQ, Zhang XX, Gong SY, Li WF. Facile synthesis of Ag/Ag_3PO_4 composites with highly efficient and stable photocatalytic performance under visible light. J Chin Chem Soc. 2017; 64: 1172-1180.
42. Zhang DF, Wang JX. In situ photoactivated plasmonic Ag_3PO_4@silver as a stable catalyst with enhanced photocatalytic activity under visible light. Mater Res. 2017; 20: 702-711.
43. Song SQ, Meng AY, Jiang SJ, Cheng B, Jiang CJ. Construction of Z-scheme Ag_2CO_3/N-doped graphene photocatalysts with enhanced visible-light photocatalytic activity by tuning the nitrogen species. Appl Surf Sci. 2017; 396: 1368-1374.
44. Luo J, Zhou XS, Zhang JQ, Du ZH. Fabrication and characterization of Ag_2CO_3/SnS_2 composites with enhanced visible-light photocatalytic activity for the degradation of organic pollutants. RSC Adv. 2015; 5: 86705-86712.
45. Wang G, Ren Y, Zhou GJ, Wang JP, Cheng HF, Wang ZY, et al. Synthesis of highly efficient visible light Ag@Ag_3VO_4 plasmonic photocatalysts. Surf Coat Technol. 2013; 228: S283-S286.
46. Meng F, Lu F, Sun Z, Lü J. A mechanism for enhanced photocatalytic activity of nano-size silver particle modified titanium dioxide thin films. Sci China Technol Sci. 2010; 53: 3027-3032.
47. Meng F, Sun Z. A mechanism for enhanced hydrophilicity of silver nanoparticles modified TiO_2 thin films deposited by RF magnetron sputtering. Appl Surf Sci. 2009; 255: 6715-6720.
48. Xu DF, Cheng B, Cao SW, Yu JG. Enhanced photocatalytic activity and stability of Z-scheme Ag_2CrO_4-GO composite photocatalysts for organic pollutant degradation. Appl Catal B. 2015; 164: 380-388.
49. Ouyang SX, Li ZS, Ouyang Z, Yu T, Ye JH, Zou ZG. Correlation of crystal structures, electronic structures, and photocatalytic properties in a series of ag-based oxides: $AgAlO_2$, $AgCrO_2$, and Ag_2CrO_4. J Phy Chem C. 2008; 112: 3134-3141.

50. Jonjana S, Phuruangrat A, Thongtem S, Thongtem T. Synthesis of AgI/Bi_2MoO_6 heterojunctions and their photoactivity enhancement driven by visible light. Mater Lett. 2016; 175: 75-78.
51. Zhu LF, Huang DQ, Ma JF, Wu DR, Yang MR, Komarneni S. Fabrication of AgBr/Ag_2CrO_4 composites for enhanced visible-light photocatalytic activity. Ceram Int. 2015; 41: 12509-12513.
52. Wu XF, Sun Y, Li H, Wang YJ, Zhang CX, Zhang JR, et al. In-situ synthesis of novel p-n heterojunction of Ag_2CrO_4/$Bi_2Sn_2O_7$ hybrids for visible-light-driven photocatalysis. J Alloys Compd. 2018; 740: 1197-1203.
53. Meng F, Wang L, Cui J. Controllable synthesis and optical properties of nano-CeO_2 via a facile hydrothermal route. J Alloys Compd. 2013; 556: 102-108.
54. Wang L, Meng F, Li K, Lu F. Characterization and optical properties of pole-like nano-CeO_2 synthesized by a facile hydrothermal method. Appl Surf Sci. 2013; 286: 269-274.
55. Wang L, Meng F. Oxygen vacancy and Ce^{3+} ion dependent magnetism of monocrystal CeO_2 nanopoles synthesized by a facile hydrothermal method. Mater Res Bull. 2013; 48: 3492-3498.
56. Meng F, Fan Z, Zhang C, Hu Y, Guan T, Li A. Morphology-controlled synthesis of CeO_2 microstructures and their room temperature ferromagnetism. J Mater Sci Technol. 2017; 33: 444-451.
57. Luo J, Zhou XS, Ma L, Xu XY. Rational construction of Z-scheme Ag_2CrO_4/g-C_3N_4 composites with enhanced visible-light photocatalytic activity. Appl Surf Sci. 2016; 390: 357-367.
58. Hamadanian M, Reisi-Vanani A, Majedi A. Preparation and characterization of S-doped TiO_2 nanoparticles, effect of calcination temperature and evaluation of photocatalytic activity. Mater Chem Phys. 2009; 116: 376-382.
59. Bi JH, Wu L, Li J, Li Z, Wang XX, Fu XZ. Simple solvothermal routes to synthesize nanocrystalline Bi_2MoO_6 photocatalysts with different morphologies. Acta Mater. 2007; 55: 4699-4705.
60. Shang YY, Chen X, Liu WW, Tan PF, Chen HY, Wu LD, et al. Photocorrosion inhibition and high-efficiency photoactivity of porous g-C_3N_4/Ag_2CrO_4 composites by simple microemulsion-assisted co-precipitation method. Appl Catal B. 2017; 204: 78-88.
61. Huang HW, Liu LY, Zhang YH, Tian N. One pot hydrothermal synthesis of a novel $BiIO_4$/Bi_2MoO_6 heterojunction photocatalyst with enhanced visible-light-driven photocatalytic activity for rhodamine B degradation and photocurrent generation. J Alloys Compd. 2015; 619: 807-811.
62. Atacan K, Güy N, Boutra B, Özacar M. Enhancement of photoelectrochemical hydrogen production by using a novel ternary Ag_2CrO_4/GO/$MnFe_2O_4$ photocatalyst. Int J Hydrog Energy. 2020; 45: 17453-17467.
63. de Mendonca VR, Mourao HA, Malagutti AR, Ribeiro C. The role of the relative dye/photocatalyst concentration in TiO_2 assisted photodegradation process. Photochem Photobiol. 2014; 90: 66-72.
64. Saeed M, Khan I, Adeel M, Akram N, Muneer M. Synthesis of a CoO-ZnO photocatalyst for enhanced visible-light assisted photodegradation of methylene blue. New J Chem. 2022; 46: 2224-2231.
65. Saeed M, Ibrahim M, Muneer M, Akram N, Usman M, Maqbool I, et al. ZnO-TiO_2: Synthesis, characterization and evaluation of photo catalytic activity towards degradation of methyl orange. Z Phys Chem. 2021; 235: 225-237.

66. Lin D, Gao MH, You LS, Li Y, Li ZY, Guo LN, et al. Fabrication of novel Ag/$AgVO_3$/WO_3 homojunction/heterojunction nanomaterials with highly enhanced photocatalytic activity-Investigation on type I plus Z-scheme mechanism. J Alloys Compd. 2020; 846: 156274.